Facile fabrication of novel Cd$_3$(C$_3$N$_3$S$_3$)$_2$/CdS porous composites and their photocatalytic performance for toluene selective oxidation under visible light irradiation

Jie He[a], Lang Chen[a,*], Du Ding[a], Ya-Kun Yang[a], Chak-Tong Au[b], Shuang-Feng Yin[a,*]

[a] State Key Laboratory of Chemo/Biosensing and Chemometrics, College of Chemistry and Chemical Engineering, Provincial Hunan Key Laboratory for Cost-effective Utilization of Fossil Fuel Aimed at Reducing Carbon-dioxide Emissions, Hunan University, Changsha, 410082, Hunan, People's Republic of China
[b] College of Chemistry and Chemical Engineering, Hunan Institute of Engineering, Xiangtan, 411104, Hunan, People's Republic of China

ABSTRACT

A simple hydrothermal approach was adopted for the construction of novel porous Cd$_3$(C$_3$N$_3$S$_3$)$_2$/CdS composites that were endowed with heterojunctions. In the synthesis, Cd$_3$(C$_3$N$_3$S$_3$)$_2$ (denoted as Cd$_3$(TMT)$_2$) was adopted as precursor, and a spontaneous self-decomposition process is responsible for the formation of heterojunctions and porous structure. By controlling the hydrothermal temperature and hence the level of Cd$_3$(TMT)$_2$ decomposition, the photocatalytic activity of the Cd$_3$(TMT)$_2$/CdS composites can be regulated. The composite prepared at 155 °C exhibits outstanding photocatalytic performance towards toluene selective oxidation to benzaldehyde, giving a benzaldehyde formation rate of 787 μmol g^{-1} h^{-1} under visible light ($\lambda \geq 420$ nm) without the need of any solvent. The excellent performance is ascribed to the unique Cd$_3$(TMT)$_2$/CdS porous structure: large in surface area and rich in heterojunctions. In photocatalysis, the large surface area of a catalyst enables enrichment of adsorbed reactants, and the presence of heterojunctions facilitates separation and transfer of photogenerated electrons and holes. It is envisaged that the method is suitable for the generation of organic/inorganic composites for photocatalytic purposes.

1. Introduction

Recently, the selective oxidation of C−H bonds has been investigated from a photocatalytic viewpoint [1–5]. The purpose is not only for solar energy utilization but also for green chemistry. The selective activation of saturated C−H bonds in alkanes or aromatics for the generation of value-added products is a significant issue in chemical industries [6–8]. It was demonstrated that heterogeneous photocatalysis has huge potential because of the low energy consumption and high selectivity to the target products [9–14]. Nonetheless, the availability of a suitable photocatalyst is the means of success.

Cadmium-based materials, e.g., inorganic CdS [15,16], CdO [17,18], CdWO$_4$ [19,20] and organic Cd$_3$(C$_3$N$_3$S$_3$)$_2$ [21] (denoted herein as Cd$_3$(TMT)$_2$, an organic cadmium coordination polymer, see **Fig. S1** in the Supporting Information, SI) are attractive photocatalysts. With direct band gap, suitable band edge positions, excellent transport properties and high electronic mobility, CdS is fascinating in photocatalysis [22,23]. To enhance light absorption ability and electron mobility, efforts were put in for the construction of CdS structures that are unique in size, shape and morphology [24–28]. In addition, CdS-

based photocatalysts containing heterojunctions such as CdS/TiO$_2$ [29,30] and CdS/Graphene [31,32] were fabricated to promote separation of charge carriers. Recently, Su and coworkers synthesized a series of porous metal oxides in a "self-formation" fashion. The approach allows fine tuning of multiple-sized porosity, resulting in enhanced light absorption ability of the materials [33–35]. Inspired by these results we embarked to develop methods for the synthesis of photocatalysts that are stable and efficient for the selective oxidation of C−H bonds.

Because of the strong oxidizing ability driven by the positive valance band position, Cd$_3$(TMT)$_2$ is an efficient photocatalyst for H$_2$O$_2$ production [21]. It is worth pointing out that there are Cd–S bondings in Cd$_3$(TMT)$_2$. If there is partial decomposition of Cd$_3$(TMT)$_2$, there would be generation of CdS and consequently Cd$_3$(TMT)$_2$/CdS heterojunctions. Also, the combined presence of Cd$_3$(TMT)$_2$ and CdS could greatly reduce the deep oxidation of organics because the valance band position of CdS is less positive than that of Cd$_3$(TMT)$_2$.

In the present work, we used a facile hydrothermal method to construct Cd$_3$(TMT)$_2$/CdS porous composites using Cd$_3$(TMT)$_2$ as precursor. We observed in situ formation of pores in the Cd$_3$(TMT)$_2$/CdS
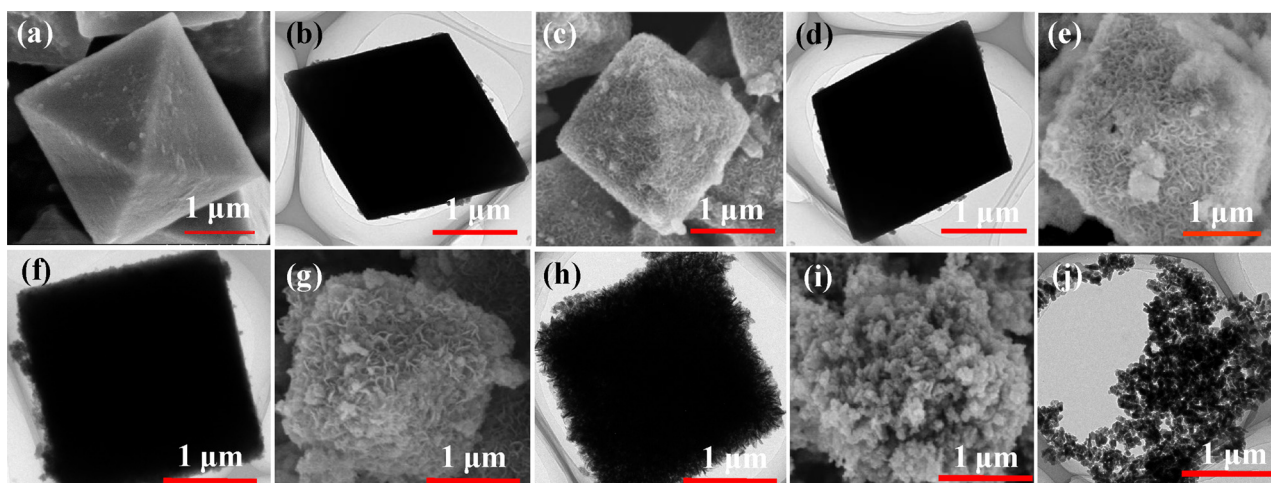
Fig. 1. SEM and TEM images of Cd$_3$(TMT)$_2$ precursor (a) (b), HT–140–Cd$_3$(TMT)$_2$ (c) (d), HT–150–Cd$_3$(TMT)$_2$ (e) (f), HT–155–Cd$_3$(TMT)$_2$ (g) (h) and HT–160–Cd$_3$(TMT)$_2$ (i) (j).

composites which is similar to that of the "self-formation" process reported by Su and co-workers [33–35]. The rate of benzaldehyde formation in the selective oxidation of toluene comes to a maximum over the optimized composite. The relationship between catalytic performance and structure of catalysts was studied.

2. Experimental

All of the reagents were commercially available and were used without further purification.

2.1. Synthesis of Cd$_3$(TMT)$_2$ micro-octahedral precursor

Cd$_3$(TMT)$_2$ micro-octahedral precursor was prepared at room temperature following the precipitation method described by Zhuang et al. [21].

2.2. Synthesis of Cd$_3$(TMT)$_2$/CdS porous composites

The prepared Cd$_3$(TMT)$_2$ precursor (0.5 g) was dispersed in 80 mL of de-ionized water by stirring (30 min) and sonication (30 min). The mixture was then transferred to a stainless steel autoclave and subjected to hydrothermal treatment at different temperatures for 5 h. Finally, the precipitate was filtered out, repeatedly washed, and dried at 80 °C overnight. The as-prepared catalysts hydrothermal treated at 140 °C, 150 °C, 155 °C and 160 °C is denoted herein as HT–140–Cd$_3$(TMT)$_2$, HT–150–Cd$_3$(TMT)$_2$, HT–155–Cd$_3$(TMT)$_2$ and HT–160–Cd$_3$(TMT)$_2$, respectively.

2.3. Characterization

The crystallinity of the prepared samples were characterized by XRD (D/MAX-2000/PC, Rigaku Corporation) with monochromatized CuKα radiation (λ = 0.15406 nm). The scanning 2θ range was 5°–80°. The surface composition was determined by X-ray photoelectron spectroscopy (XPS). The scanning electron microscope (SEM) images were collected over a field emission scanning electron microscope (FE-SEM) (Hitachi S-4800). A transmission electron microscope (TEM, TecnaiG2 F20, operated at accelerating voltage of 200 kV) was used to obtain morphologic and energy dispersive X-ray spectroscopic data. The BET surface area was measured using a Gemini VII 2390 instrument (Micromeritics Instrument Corp.). The UV–vis diffuse reflectance spectroscopic (UV–vis DRS) investigation was conducted over a Cary 100 (Agilent) spectrophotometer. Photoelectrochemical activity measurements were recorded employing an electrochemical analyser

(CHI660E, Shanghai Chenhua electrochemical workstation) over a standard three-electrode system using the to-be-measured sample as working electrode, a Pt wire as counter electrode, and a saturated calomel electrode (SCE) as reference electrode. Mott-Schottky experiments were performed in a sodium sulphate electrolyte solution (0.2 M) (pH = 6.8), and the perturbation signals were 10 mV at a frequency of 1 kHz.

2.4. Photocatalytic conversion of toluene

Briefly, 1 mL of substrate and 50 mg of photocatalyst were uniformly mixed in a round bottom flask with a condenser pipe on top. Then O$_2$ was bubbled through the mixture at a rate of 1.5 mL min^{-1}. The suspension was stirred for 30 min before illumination. Then the reaction was carried out under visible light originated from a 300 W Xe lamp (PLS-SXE 300 C, Perfectlight) with a 420 nm cut off filter. After reaction, the catalyst was removed by centrifugation, and the products were directly analyzed with an SHIMADZU Gas Chromatograph (GC-2010, with a capillary SH-Rtx-1701 column). Control experiments were conducted with the addition of 1 mmol of selected scavengers for the quenching of specific species. Tetra-methylpiperidine N-oxide (TEMPO) was used as radical scavenger. Ammonium oxalate (AO), potassium persulfate (K$_2$S$_2$O$_8$), tert-butyl alcohol (TBA) and benzoquinone (BQ) were used as scavengers for photogenerated holes, photogenerated electrons, hydroxyl radicals, and superoxide radicals, respectively. The conversion and selectivity are defined as:

$$Conversion(\%) = \frac{\sum amount of each product (mmol)}{amount of substrate (mmol)} \times 100\% \quad (1)$$

$$Selectivity(\%) = \frac{amount of corresponding aldehyde (mmol)}{\sum amount of each product (mmol)} \times 100\% \quad (2)$$

3. Results and discussion

3.1. Morphological structure

The SEM and TEM images of as-prepared catalysts are shown in Fig. 1. The Cd$_3$(TMT)$_2$ precursor is in the form of micro-octahedrons (Fig. 1a,b and **Fig. S2** (SI)). The triangular surfaces of the octahedrons are sporadically covered by a number of nanoparticles that are irregular in shape. As for the Cd$_3$(TMT)$_2$/CdS composites, there is roughening of surface and obvious presence of pores (Fig. 1c–j). An increase of hydrothermal temperature from 140 to 155 °C results in more pores on the surfaces. When the hydrothermal temperature is 160 °C, there is

Table 1
BET surface areas of $Cd_3(TMT)_2$, $HT–140–Cd_3(TMT)_2$, $HT–155–Cd_3(TMT)_2$ and $HT–160–Cd_3(TMT)_2$.

Catalyst	S_{BET} (m^2/g)	Total pore volume (cm^3/g)
$Cd_3(TMT)_2$	2.0	12.7
$HT–140–Cd_3(TMT)_2$	3.9	21.0
$HT–150–Cd_3(TMT)_2$	40.5	31.1
$HT–155–Cd_3(TMT)_2$	109.9	38.4
$HT–160–Cd_3(TMT)_2$	38.5	50.0

breakdown of the octahedral structure to small particles (Fig. 1i and j). As shown in Fig. S3, the N_2 adsorption/desorption isotherm of $HT–150–Cd_3(TMT)_2$ and $HT–155–Cd_3(TMT)_2$ could be considered as Type III (according to the IUPAC classification) with a type H3 hysteresis loop starting from $P/P_0 = 0.4$. The pore size distribution curve (inset of Fig. S3) demonstrates presence of mesopores and macropores.

A comparison of the BET surface areas and SEM images of $Cd_3(TMT)_2$, $HT–140–Cd_3(TMT)_2$, $HT–150–Cd_3(TMT)_2$, $HT–155–Cd_3(TMT)_2$ and $HT–160–Cd_3(TMT)_2$ reveals that $HT–155–Cd_3(TMT)_2$ is the largest in surface area (Table 1). Thus, it is apparent that there is in situ generation of pores during the hydrothermal processes. We propose a plausible mechnism for in-situ formation of CdS through the transformation of $Cd_3(TMT)_2$. As shown in Scheme 1, there are no pores on the surface of $Cd_3(TMT)_2$ micro-octahedron. When the hydrothermal treatment begins, there is $Cd_3(TMT)_2$ decomposition. It is deduced that the weak Cd−S chemical bond breaks first, and there is dissolution of Cd^{2+} in water. With the increase of temperature, the breaking of C−S bond resultes in in-situ formation of CdS. Meanwhile, the triazine ring structure of $Cd_3(TMT)_2$ breaks down under hydrothermal condition with the release of gas products such as CO_2 and nitrogen oxides. Similar to the "self-formation" phenomenon reported by Su and co-workers [33–35], pores are spontaneously generated during the escape of gases from the interior of the octahedron structures. Therefore, the $HT–155–Cd_3(TMT)_2$ composite with octahedral structure is porous. However, when the hydrothermal temperature is 160 °C, there is total breakdown of the octahedral structure to small CdS particles.

3.2. Catalyst composition

The XRD patterns of the catalysts prepared by hydrothermal treatment of $Cd_3(TMT)_2$ are shown in Fig. 2a. The peaks of $HT–140–Cd_3(TMT)_2$ are almost the same as those of $Cd_3(TMT)_2$. As for $HT–150–Cd_3(TMT)_2$, the characteristic peaks of $Cd_3(TMT)_2$ decrease in intensity and there is the detection of peaks attributable to hexagonal

CdS. This trend becomes more obvious in the case of $HT–155–Cd_3(TMT)_2$. Over $HT–160–Cd_3(TMT)_2$, only the peaks of hexagonal CdS can be observed. Thus, the $HT–150–Cd_3(TMT)_2$ and $HT–155–Cd_3(TMT)_2$ catalysts are likely to be the ones that have $Cd_3(TMT)_2$–CdS heterojunctions. Indeed, the presence of heterojuctions is confirmed by the HRTEM images (Fig. 2c). The edge lattice fringes are confirmed by the selected area electron diffraction (SAED) pattern of $Cd_3(TMT)_2$ [21,36,37]. In close contact with $Cd_3(TMT)_2$ is a lattice with a spacing of 0.32 nm, which corresponds to the (002) plane of hexagonal CdS (JCPDS 41-1049).

In order to confirm the decomposition of $Cd_3(TMT)_2$ to CdS, N1s XPS spectra of $Cd_3(TMT)_2$ and $HT–160–Cd_3(TMT)_2$ were recorded (Fig. 2b). The peak at 399.5 eV detected over the former is typical of sp2-bonded N in triazine rings (C−N−C) of $Cd_3(TMT)_2$. There is no detection of N element over the $HT–160–Cd_3(TMT)_2$ sample which confirms the complete transformation of $Cd_3(TMT)_2$ to CdS. In addition, the FT-IR spectra (Fig. 2d) of $Cd_3(TMT)_2$ and $HT–140–Cd_3(TMT)_2$ show peaks at 800–1650 cm^{-1} typical of s-triazine ring system (breathing mode) and heterocycles (stretching vibration modes of C=N and C−N). However, over $HT–150–Cd_3(TMT)_2$, $HT–155–Cd_3(TMT)_2$ and $HT–160–Cd_3(TMT)_2$, those typical peaks greatly decrease in intensity and finally only peaks typical of CdS can be detected. The results of FT-IR characterization confirm the decomposition of $Cd_3(TMT)_2$ to CdS during the hydrothermal process. Moreover, the results of EDX analysis indicate that the mass percentage of $Cd_3(TMT)_2$ in $HT–140–Cd_3(TMT)_2$, $HT–150–Cd_3(TMT)_2$ $HT–155–Cd_3(TMT)_2$ is 82.6%, 54.0%, and 26.3%, respectively (Table 2). As for $HT–160–Cd_3(TMT)_2$, it is mostly CdS.

3.3. Optical property

It is important to figure out the light absorption property of the catalysts because it is directly related to photocatalytic performance. The ultraviolet visible diffuse reflectance spectra of the samples are shown in Fig. 3a. All of them exhibit absorption both in the UV and visible-light regions. With higher hydrothermal temperature for catalyst preparation, there is red shift of absorption edges.

We calculated the value of band gap energies (Fig. 3b) of the samples using the $(\alpha h\nu)^n = A(h\nu - E_g)$ formula, where α, h, ν, E_g, and A are the absorption coefficient, Plank constant, light frequency, band gap, and a constant [38]. The obtained E_g values are 2.78, 2.68, 2.62, 2.44 and 2.40 eV for $Cd_3(TMT)_2$, $HT–140–Cd_3(TMT)_2$, $HT–150–Cd_3(TMT)_2$, $HT–155–Cd_3(TMT)_2$ and $HT–160–Cd_3(TMT)_2$, respectively.

We carried out electrochemical analysis to investigate the band structure of the $Cd_3(TMT)_2$ and CdS. The typical Mott-Schottky plot of
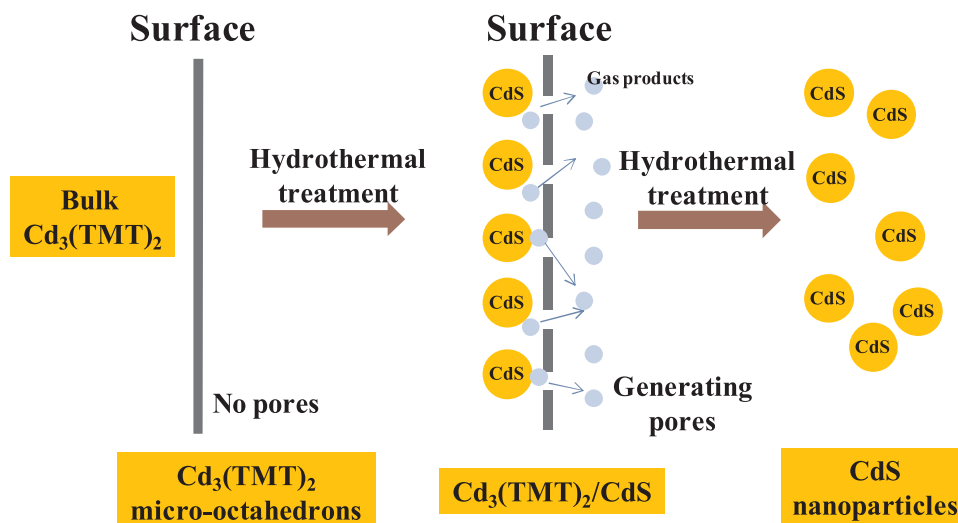
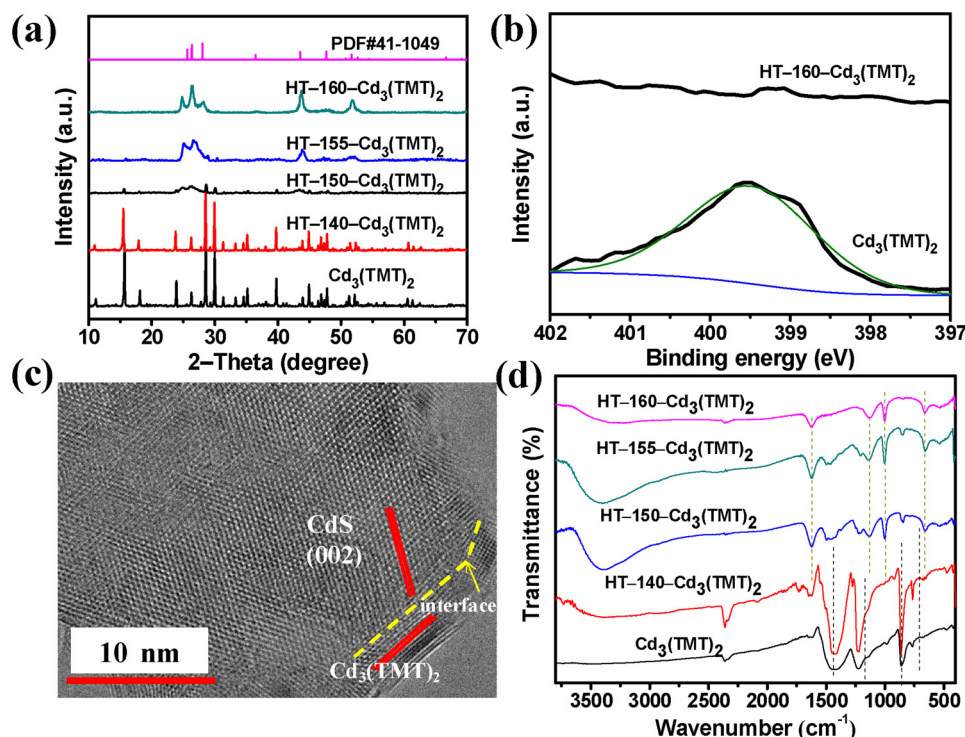**Scheme 1.** Schematic of the plausible decomposition process of $Cd_3(TMT)_2$.

Fig. 2. (a) XRD patterns of $Cd_3(TMT)_2$, HT–140–$Cd_3(TMT)_2$, HT–150–$Cd_3(TMT)_2$, HT–155–$Cd_3(TMT)_2$ and HT–160–$Cd_3(TMT)_2$, (b) N1s XPS spectra of $Cd_3(TMT)_2$ and HT–160–$Cd_3(TMT)_2$, (c) HRTEM images of HT–155–$Cd_3(TMT)_2$ and (d) FT-IR spectra of $Cd_3(TMT)_2$, HT–140–$Cd_3(TMT)_2$, HT–150–$Cd_3(TMT)_2$, HT–155–$Cd_3(TMT)_2$ and HT–160–$Cd_3(TMT)_2$.

Table 2

Content of Cd element detected by EDX and calculated weight content of $Cd_3(TMT)_2$ in the as-prepared catalysts.

Catalyst	Content of Cd element detected by EDX (wt%)	Calculated content of $Cd_3(TMT)_2$ (wt%)
$Cd_3(TMT)_2$	49.3	100
HT–140–$Cd_3(TMT)_2$	54.1	82.6
HT–150–$Cd_3(TMT)_2$	62.3	54.0
HT–155–$Cd_3(TMT)_2$	70.2	26.3
HT–160–$Cd_3(TMT)_2$	78.1	0

$Cd_3(TMT)_2$ in the dark (Fig. 3c) shows a positive slope of C^{-2}–E plot, which is an indication of n-type semiconductor. The flat-band potential (Vfb) of about -0.74 V vs. NHE at pH 7.0 is determined through extrapolation to the X intercept in the Mott-Schottky plot. By combining with the band-gap energy of ca. 2.78 eV estimated from the optical absorption, the valence band position of $Cd_3(TMT)_2$ is calculated to be 2.04 V vs. NHE at pH 7.0. The valence band position of HT–160–$Cd_3(TMT)_2$ (CdS) is calculated to be 2.08 V vs. NHE at pH 7.0 using the same method. In view of the special heterojucntion-enriched porous structures and the optical properties of the catalysts, it is expected that a combination of $Cd_3(TMT)_2$ with CdS could results in improvement of photocatalytic activity because of the enhanced adsorption of reactants and high seperation rate of charge carriers.

3.4. Photocatalytic property

The photocatalytic selective oxidation of toluene for the generation of benzaldehyde was adopted as a model reaction. Previously, we reported a green process for the selective oxidation of alkanes using flower-like Bi_2WO_6 [39] as active photocatalyst, but its poor stability in the absence of solvents restricts its application. The results of the present study (Table 3, entries 1–3) indicate that the oxidation process is photocatalytic and the presence of O_2 is indispensable. It is observed that $Cd_3(TMT)_2$ is not active (entry 4) while the $Cd_3(TMT)_2$/CdS composites exhibit fairly high selective oxidation efficiency (entries 5–8). Among the catalysts in a span of 3 h, HT–155–$Cd_3(TMT)_2$ shows the

highest toluene conversion (1.3%) and efficiency for benzaldehyde formation (rate $= 787$ mmol $g^{-1} h^{-1}$) without the need of any solvent, a performance better than that of flower-like Bi_2WO_6 under similar reaction conditions. It is noted that a hydrothermal temperature of 155 °C for catalyst preparation is the most suitable for the optimization of toluene conversion. It is because the generation of CdS from the partial decomposition of $Cd_3(TMT)_2$ results in the formation of heterojuctions between $Cd_3(TMT)_2$ and CdS that are beneficial for fast separation of charge carriers. We also tested the activity of a sample of mechanically mixed $Cd_3(TMT)_2$ and CdS (26.3 wt% of $Cd_3(TMT)_2$), and the formation rate of benzaldehyde is only one-seventh of that of HT–155–$Cd_3(TMT)_2$ (entry 9). The result confirms that the self-formed unique structure is essential for the high activity. However, at a hydrothermal temperature of 160 °C, the HT–160–$Cd_3(TMT)_2$ sample is mainly composed of CdS nanoparticles that is poor in photocatalytic activity. As shown in **Table S1** (SI), although there is variation in factors such as light intensity, catalyst loading, HT–155–$Cd_3(TMT)_2$ exhibits better benzaldehyde formation rate than most of the reported catalysts except Pd/Bi_2WO_6. However, noble metal is necessary in the Pd/Bi_2WO_6 catalytic system which is expensive. The recyclability of HT–155–$Cd_3(TMT)_2$ is shown in **Fig. S4**a (SI), and there is no significant loss of activity across a test of 5 runs. The results are further confirmed by careful characterization of the catalyst before and after the photocatalytic reaction using the XRD technique, and it is confirmed that there is no change of phase structure (**Fig. S4**b, SI) during the reaction. As shown in **Scheme S2**, under visible light irradiation the photogenerated electrons migrate from the conduction band of $Cd_3(TMT)_2$ to that of CdS, and the holes migrate from the valence band of CdS to that of $Cd_3(TMT)_2$. In this way, a long-lived electron-transfer state is established and there are less holes (h^+) accumulated at the valence band of CdS. Therefore, the stability of $Cd_3(TMT)_2$/CdS is greatly enhanced in comparison with that of pure CdS. Moreover, HT–155–$Cd_3(TMT)_2$ is also effective for the selective oxidation of toluene derivatives (**Scheme S1**, SI). Compared with the oxidation of toluene, the transformation of chlorotoluene is less significant; the phenomenon can be associated with the presence of an electron withdrawing group (–Cl) that hinders the oxidation of the methyl group [39,40]. In the case of xylene, there is the generation of the
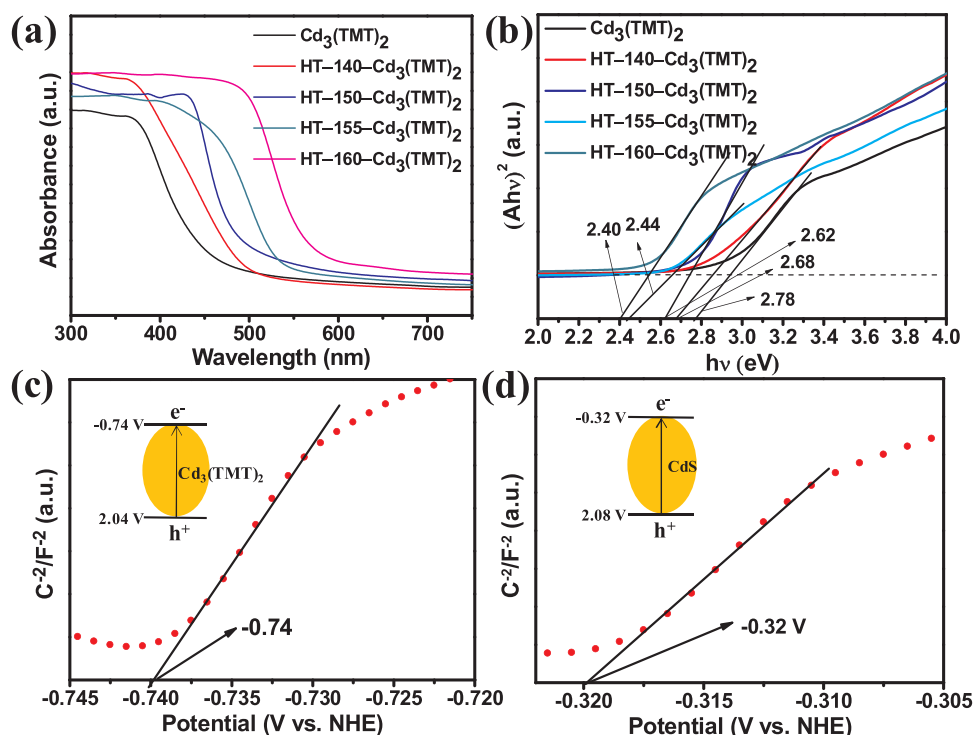
Fig. 3. (a) UV–vis absorption property of the prepared catalysts, (b) the corresponding $(Ah\nu)^2$ versus photon energy plots, Mott-Schottky plot of (c) $Cd_3(TMT)_2$ and (d) CdS, the inset in (c) and (d) are the derived band structures.

Table 3
Selective oxidation of toluene to benzaldehyde over the prepared samples[a].

Entry	Catalyst	Conv. (%)	Benzaldehyde	
			formation rate ($\mu mol\,g^{-1}\,h^{-1}$)	Sel. (%)
1	None	–	–	–
2[b]	HT–155–$Cd_3(TMT)_2$	–	–	–
3[c]	HT–155–$Cd_3(TMT)_2$	–	–	–
4	$Cd_3(TMT)_2$	–	trace	–
5	HT–140–$Cd_3(TMT)_2$	0.2	115	95.6
6	HT–150–$Cd_3(TMT)_2$	0.9	575	97.6
7	HT–155–$Cd_3(TMT)_2$	1.3	787	98.5
8	HT–160–$Cd_3(TMT)_2$	0.8	449	94.5
9[d]	mixture	0.3	168	96.7
10[e]	Flower-like Bi_2WO_6	1.5	464	96

[a] Photocatalyst (50 mg), substrate (1 mL), no solvent, room temperature, O_2 flow rate (1.5 mL min^{-1}), visible-light irradiation ($\lambda \geq 420$ nm, 3 h).

[b] Replacing O_2 with N_2.

[c] Without irradiation.

[d] Mechanical mixing of $Cd_3(TMT)_2$ and CdS with 26.3 wt% $Cd_3(TMT)_2$.

[e] Ref. [39], catalyst (50 mg), substrate (8 mmol), O_2 flow rate (3 mL min^{-1}), visible-light irradiation ($\lambda \geq 400$ nm, 5 h).

corresponding alcohol as by-product. In all cases of using HT–155–$Cd_3(TMT)_2$, there is no detection of carbon dioxide, indicating the absence of over oxidation.

To understand the role of radical species involved in the photocatalytic selective oxidation of toluene over HT–155–$Cd_3(TMT)_2$, we performed experiments with the addition of scavengers for the quenching of hydroxyl radicals ($\cdot$OH), superoxide radicals ($O_2\cdot^-$), holes (h^+), and electrons (e^-) (**Fig. S5**, SI). When using tetra-methyl-piperidine N-oxide (TEMPO), it shows only minute conversion of toluene. When ammonium oxalate (AO) is added as hole scavenger, the conversion of toluene is almost quenched and there is no increase of conversion with time. The results indicate that the presence of holes is indispensable for the activation of toluene. When benzoquinone (BQ) is

added to quench superoxide radicals, the conversion of toluene is significantly inhibited. Such a phenomenon is also observed when $K_2S_2O_8$ is added as electron scavenger. It is known that the quenching of electrons results in poor formation of superoxide radicals which are produced through the activation of molecular oxygen by photogenerated electrons. Thus, it is understandable that the conversion of toluene can be significant inhibited by both BQ and $K_2S_2O_8$. Furthermore, the addition of tert-butyl alcohol (TBA) as scavenger for hydroxyl radicals has little effect on toluene conversion. The results clearly suggest that the photogenerated holes play a predominant role in the photocatalytic oxidation of toluene over HT–155–$Cd_3(TMT)_2$.

3.5. Possible mechanism for photocatalysis

Based on the above discussions, a reaction mechanism is proposed (**Scheme S2**, SI). Under visible light irradiation, there is the generation of electron–hole pairs, and the toluene adsorbed on the surface of HT–155–$Cd_3(TMT)_2$ is oxidized to cationic radicals by the positive holes. The photogenerated electrons migrate from the conduction band of $Cd_3(TMT)_2$ to that of CdS, thus establishing a long-lived electron-transfer state. Meanwhile, the electrons react with adsorbed O_2 to give activated oxygen species (e.g., $O_2\cdot^-$). The activated oxygen species then selectively oxidize the cationic radicals, leading to the formation of benzaldehyde.

It was found that the photocurrent generated in HT–155–$Cd_3(TMT)_2$ under visible light irradiation is the highest among the samples, indicating the generation of photo-induced electrons in HT–155–$Cd_3(TMT)_2$ is the most efficient (**Fig. 4**a). Furthermore, the arc radius of the electrochemical impedance spectroscopic (EIS) plot of HT–155–$Cd_3(TMT)_2$ is the smallest, demonstrating that HT–155–$Cd_3(TMT)_2$ has the highest charge-transfer ability among the samples (**Fig. 4**b). Moreover, it is revealed from the band characteristics (inset of **Scheme S2**, SI) that the light-excited electrons (e^-) that are transferred to the conduction band of CdS are thermodynamically able to reduce O_2 (E ($O_2/O_2\cdot^-$) = -0.16 V), and yet the potential of the photogenerated holes in the valence band is inadequate to oxidize OH^- to hydroxyl radicals (E ($OH^-/\cdot OH$) = 2.4 V). With the absence of $\cdot$OH (an
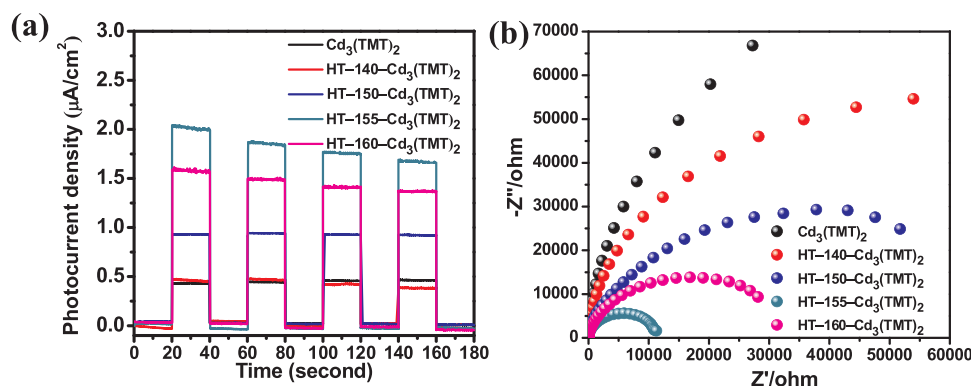
Fig. 4. (a) Photocurrent response under visible-light irradiation and (b) electrochemical impedance spectroscopy of $Cd_3(TMT)_2$, HT–140–$Cd_3(TMT)_2$, HT–150–$Cd_3(TMT)_2$ HT–155–$Cd_3(TMT)_2$ and HT–160–$Cd_3(TMT)_2$.

agent common for deep oxidation), HT–155–$Cd_3(TMT)_2$ is efficient for the selective oxidation of alkanes.

4. Conclusions

In summary, porous $Cd_3(TMT)_2$/CdS composites endowed with heterojunctions were facilely synthesized by hydrothermal treatment using $Cd_3(TMT)_2$ as precursor. When used as photocatalyst, the HT–155–$Cd_3(TMT)_2$ composite exhibits excellent performance towards the conversion of toluene to benzaldehyde. The superior performance arises from a proper combination of band structures and enhanced separation of charge carriers. It is envisaged that the method is also suitable for the construction of other porous organic/inorganic heterojunctions.

Acknowledgments

Appendix A. Supplementary data

Supplementary material related to this article can be found, in the online version, at doi:https://doi.org/10.1016/j.apcatb.2018.04.008.

References

[1] X.Q. Hu, J.R. Chen, W.J. Xiao, Controllable remote C−H bond functionalization by visible-light photocatalysis, Angew. Chem. Int. Ed. 56 (2017) 1960–1962.

[2] D.X. Yang, T.B. Wu, C.J. Chen, W.W. Guo, H.Z. Liu, B.X. Han, The highly selective aerobic oxidation of cyclohexane to cyclohexanone and cyclohexanol over V_2O_5@TiO_2 under simulated solar light irradiation, Green Chem. 19 (2017) 311–318.

[3] Y. Shiraishi, S. Shiota, H. Hirakawa, S. Tanaka, S. Ichikawa, T. Hirai, Titanium dioxide/reduced graphene oxide hybrid photocatalysts for efficient and selective partial oxidation of cyclohexane, ACS Catal. 7 (2017) 293–300.

[4] A. Henriquez, H.D. Mansilla, A. Martinez Martinez-de la Cruz, J. Freer, D. Contreras, Selective oxofunctionalization of cyclohexane over titanium dioxide–based and bismuth oxyhalide (BiOX, X = Cl⁻, Br⁻, I⁻) photocatalysts by visible light irradiation, Appl. Catal. B Environ. 206 (2017) 252–262.

[5] S. Verma, R.B.N. Baig, M.N. Nadagouda, R.S. Varma, Photocatalytic C–H activation of hydrocarbons over VO@g-C_3N_4, ACS Sustainable Chem. Eng. 4 (2016) 2333–2336.

[6] S. Senaweera, J.D. Weaver, C.–F. Dual, C–H functionalization via photocatalysis: access to multifluorinated biaryls, J. Am. Chem. Soc. 138 (2016) 2520–2523.

[7] R.H. Liu, H. Huang, H.T. Li, Y. Liu, J. Zhong, Y.Y. Li, S. Zhang, Z.H. Kang, Metal nanoparticle/carbon quantum dot composite as a photocatalyst for high-efficiency cyclohexane oxidation, ACS Catal. 4 (2014) 328–336.

[8] Y.H. Zhang, N. Zhang, Z.R. Tang, Y.J. Xu, Transforming CdS into an efficient visible light photocatalyst for selective oxidation of saturated primary C–H bonds under ambient conditions, Chem. Sci. 3 (2012) 2812–2822.

[9] W.F. Wu, X.L. He, Z.H. Fu, Y.C. Liu, Y.L. Wang, X.L. Gong, X.L. Deng, H.T. Wu, Y.H. Zou, N.Y. Yu, D.L. Yin, Metal chlorides-catalyzed selective oxidation of cyclohexane by molecular oxygen under visible light irradiation, J. Catal. 286 (2012) 6–12.

[10] H. Hattori, Y. Ide, S. Ogo, K. Inumaru, M. Sadakane, T. Sano, Efficient and selective photocatalytic cyclohexane oxidation on a layered titanate modified with iron oxide under sunlight and CO_2 atmosphere, ACS Catal. 2 (2012) 1910–1915.

[11] S.P. Tang, W.F. Wu, Z.H. Fu, S. Zou, Y.C. Liu, H.H. Zhao, S.R. Kirk, D.L. Yin, Vanadium–substituted tungstophosphoric acids as efficient catalysts for visible–light–driven oxygenation of cyclohexane by dioxygen, ChemCatChem 7 (2015) 2637–2645.

[12] J. Ding, W. Xu, H. Wan, D.S. Yuan, C. Chen, L. Wang, G.F. Guan, W.L. Dai, Nitrogen vacancy engineered graphitic C_3N_4-based polymers for photocatalytic oxidation of aromatic alcohols to aldehydes, Appl. Catal. B Environ. 221 (2018) 626–634.

[13] J. Ding, L. Zhang, Q.Q. Liu, W.L. Dai, G.F. Guan, Synergistic effects of electronic structure of WO_3 nanorods with the dominant {001} exposed facets combined with silver size-dependent on the visible-light photocatalytic activity, Appl. Catal. B Environ. 203 (2017) 335–342.

[14] Y.Y. Wang, W.J. Yang, X.J. Chen, J. Wang, Y.F. Zhu, Photocatalytic activity enhancement of core-shell structure g-C_3N_4@TiO_2 via controlled ultrathin g-C_3N_4 layer, Appl. Catal. B Environ. 220 (2018) 337–347.

[15] Q. Li, X. Li, S. Wageh, A.A. Al-Ghamdi, J.G. Yu, CdS/graphene nanocomposite photocatalysts, Adv. Energy Mater. 5 (2015) 1500010.

[16] Z.R. Tang, B. Han, C. Han, Y.J. Xu, One dimensional CdS based materials for artificial photoredox reactions, J. Mater. Chem. A 5 (2017) 2387–2410.

[17] K. Karthik, S. Dhanuskodi, C. Gobinath, S. Prabukumar, S. Sivaramakrishnan, Photocatalytic and antibacterial activities of hydrothermally prepared CdO nanoparticles, J. Mater. Sci. Mater. El. 28 (2017) 11420–11429.

[18] V.K. Gupta, A. Fakhri, S. Tahami, S. Agarwal, Zn doped CdO nanoparticles: structural, morphological, optical, photocatalytic and anti-bacterial properties, J. Colloid Interf. Sci. 504 (2017) 164–170.

[19] D. Li, X.J. Bai, J. Xu, X.G. Ma, Y.F. Zhu, Synthesis of $CdWO_4$ nanorods and investigation of the photocatalytic activity, Phys. Chem. Chem. Phys. 16 (2014) 212–218.

[20] W.M. Tong, L.P. Li, W.B. Hu, T.J. Yan, G.S. Li, Systematic control of monoclinic $CdWO_4$ nanophase for optimum photocatalytic activity, J. Phys. Chem. C 114 (2010) 1512–1519.

[21] H.Q. Zhuang, L.F. Yang, J. Xu, F.Y. Li, Z.Z. Zhang, H.X. Lin, J.L. Long, X.X. Wang, Robust photocatalytic H_2O_2 production by octahedral $Cd_3(C_3N_3S_3)_2$ coordination polymer under visible light, Sci. Rep. 5 (2015) 16947.

[22] I. Majeed, M.A. Nadeem, M. Al-Oufi, M.A. Nadeem, G.I.N. Waterhouse, A. Badshah, J.B. Metson, H. Idriss, On the role of metal particle size and surface coverage for photo-catalytic hydrogen production: a case study of the Au/CdS system, Appl. Catal. B Environ. 182 (2016) 266–276.

[23] L. Shang, B.A. Tong, H.J. Yu, G.I.N. Waterhouse, C. Zhou, Y.F. Zhao, M. Tahir, L.Z. Wu, C.H. Tung, T.R. Zhang, CdS nanoparticle–decorated Cd nanosheets for efficient visible ligh–driven photocatalytic hydrogen evolution, Adv. Energy Mater. 6 (2016) 1501241.

[24] Y.X. Pan, T.H. Zhou, J.Y. Han, J.D. Hong, Y.B. Wang, W. Zhang, R. Xu, CdS quantum dots and tungsten carbide supported on anatase–rutile composite TiO_2 for highly efficient visible-light-driven photocatalytic H_2 evolution from water, Catal. Sci. Technol. 6 (2016) 2206–2213.

[25] Z.M. Zhang, C.T. Gao, Z.M. Wu, W.H. Han, Y.L. Wang, W.B. Fu, X.D. Li, E.Q. Xie, Toward efficient photoelectrochemical water-splitting by using screw-like SnO_2 nanostructures as photoanode after being decorated with CdS quantum dots, Nano Energy 19 (2016) 318–327.

[26] M. Fujishima, Y. Nakabayashi, K. Takayama, H. Kobayashi, H. Tada, High coverage formation of CdS quantum dots on TiO_2 by the photocatalytic growth of preformed seeds, J. Phys. Chem. C 120 (2016) 17365–17371.

[27] S.Q. Liu, Z.R. Tang, Y.G. Sun, J.C. Colmenares, Y.J. Xu, One-dimension-based spatially ordered architectures for solar energy conversion, Chem. Soc. Rev. 44 (2015) 5053–5075.

[28] Z.M. Bai, X.Q. Yan, Y. Li, Z. Kang, S.Y. Cao, Y. Zhang, 3D-branched ZnO/CdS

nanowire arrays for solar water splitting and the service safety research, Adv. Energy Mater. 6 (2016) 1501459.

[29] D.R. Baker, P.V. Kamat, Photosensitization of TiO$_2$ nanostructures with CdS quantum dots: particulate versus tubular support architectures, Adv. Funct. Mater. 19 (2009) 805–811.

[30] W.T. Sun, Y. Yu, H.Y. Pan, X.F. Gao, Q. Chen, L.M. Peng, CdS quantum dots sensitized TiO$_2$ nanotube-array photoelectrodes, J. Am. Chem. Soc. 130 (2008) 1124–1125.

[31] Z. Chen, S.Q. Liu, M.Q. Yang, Y.J. Xu, Synthesis of uniform CdS nanospheres/graphene hybrid nanocomposites and their application as visible light photocatalyst for selective reduction of nitro organics in water, ACS Appl. Mater. Inter. 5 (2013) 4309–4319.

[32] J.J. Yan, K. Wang, H. Xu, J. Qian, W. Liu, X.W. Yang, H.M. Li, Visible-light photocatalytic efficiencies and anti-photocorrosion behavior of CdS/graphene nanocomposites: evaluation using methylene blue degradation, Chin. J. Catal. 34 (2013) 1876–1882.

[33] X.Y. Yang, A. Leonard, A. Lemaire, G. Tian, B.L. Su, Self-formation phenomenon to hierarchically structured porous materials: design, synthesis, formation mechanism and applications, Chem. Commun. 47 (2011) 2763–2786.

[34] X.Y. Li, L.H. Chen, Y. Li, J.C. Rooke, C. Wang, Y. Lu, A. Krief, X.Y. Yang, B.L. Su, Self-generated hierarchically porous titania with high surface area: photocatalytic activity enhancement by macrochannel structure, J. Colloid Interf. Sci. 368 (2012) 128–138.

[35] X.Y. Yang, L.H. Chen, Y. Li, J.C. Rooke, C. Sanchez, B.L. Su, Hierarchically porous materials: synthesis strategies and structure design, Chem. Soc. Rev. 46 (2017) 481–558.

[36] C. Liu, H.J. Zhu, Y.S. Zhu, P.Y. Dong, H.J. Hou, Q.X. Xu, X.W. Chen, X.G. Xi, W.H. Hou, Ordered layered N-doped KTiNbO$_5$/g-C$_3$N$_4$ heterojunction with enhanced visible light photocatalytic activity, Appl. Catal. B Environ. 228 (2018) 54–63.

[37] Q. Wang, W. Wang, L.L. Zhong, D.M. Liu, X.Z. Cao, F.Y. Cui, Oxygen vacancy-rich 2D/2D BiOCl-g-C$_3$N$_4$ ultrathin heterostructure nanosheets for enhanced visible-light-driven photocatalytic activity in environmental remediation, Appl. Catal. B Environ. 220 (2018) 290–302.

[38] P. Sippel, D. Denysenko, A. Loidl, P. Lunkenheimer, G. Sastre, D. Volkmer, Dielectric relaxation processes, electronic structure, and band gap engineering of MFU-4-type metal-organic frameworks: towards a rational design of semiconducting microporous materials, Adv. Funct. Mater. 24 (2014) 3885–3896.

[39] Y. Liu, L. Chen, Q. Yuan, J. He, C.T. Au, S.F. Yin, A green and efficient photocatalytic route for the highly-selective oxidation of saturated alpha-carbon C−H bonds in aromatic alkanes over flower-like Bi$_2$WO$_6$, Chem. Commun. 52 (2016) 1274–1277.

[40] Y. Xu, Z.C. Fu, S. Cao, Y. Chen, W.F. Fu, Highly selective oxidation of sulfides on a CdS/C$_3$N$_4$ catalyst with dioxygen under visible-light irradiation, Catal. Sci. Technol. 7 (2017) 587–595.